

Antimonene with Topological Nontrivial Band Structure on Al(111) Substrate

Yang Wang^{1,†,*}

AFFILIATIONS

¹*Department of Physics, Hebei Normal University, Shijiazhuang 050024, China*

E-mail: 790814014@qq.com

Abstract

Large-area, high-quality antimonene monocrystalline polygons without an alloy layer can be automatically synthesized on Al(111) substrate at room temperature. Additionally, a previously unpredicted Kagome lattice structure of antimonene is discovered. The absorption site between the substrate and the antimonene monolayer is determined through diffraction patterns obtained by varying the incident direction of the electron beam during the deposition process. Upon confirming the structure, an experimental measurement reveals a Dirac point at Γ near -1.2 eV, providing experimental verification that antimonene belongs to the class of two-dimensional topological insulators. This classification holds great potential for the next generation of electronic devices due to its distinctive electron transport properties and spin characteristics. Furthermore, first-principles calculations are utilized to verify the type of interaction force between each atom and the electronic structures of bulk states. These calculations reveal that the electron cloud in bulk state remains delocalized, which can lead to a low dispersion band structure near the Fermi level that has significant physical implications to electronic properties and transport characteristics.

Keywords: STM, ARPES, antimonene, boundary state, band structure

1.Introduction

Two-dimensional (2D) crystals are a special type of materials that are significantly thinner than the traditional crystalline materials, and have periodic structure with no free bonds on the surface. As one of the 2D materials, graphene has drawn significant attention for its extraordinary properties, so the 2D materials with

same rotational symmetry also have been extensively explored [1-4]. Group-V elemental monolayers [5] include black and blue phosphorene [6, 7], arsenene, antimonene [8, 9] and bismuthene [10]. In particular, antimonene has attracted academic interest for its tunable band gap [8].

The stability of antimonene in the phases of α - and β - are confirmed through the phonon dispersion calculations [11]. Antimonene can be synthesized via various methods, such as antimonene polygons in β -phase can be synthesized on mica substrates via van der Waals epitaxy without alloy layer [12]. Furthermore, employing molecular beam epitaxy (MBE), both α -Sb and β -Sb have been successfully fabricated on Ag(111) [13], Cu(111) [14], and Au(111) substrate [15]. Nevertheless, for antimonene overlaid on a surface covered with an alloy layer [16, 17] above those noble metal substrates, this may cause the loss of some novel properties, because β -Sb in free standing has been theoretically predicted to be a 2D topological insulator in critical buckling angle [18] and lattice constant [19] by the density functional theory (DFT). Nevertheless, this conclusion lacks experimental confirmation. The boundary state of a topological insulator is characterized by the Dirac cone [20], which has a great potential for the next generation of electronic equipment for its high conductive properties. But among all the 2D materials, only Dirac cones in graphene have been reliably confirmed by experiments so far [2]. Another special electronic structure exhibiting a dispersionless characteristic in the momentum space named flat band (FB) also has many interesting properties [21]. The FB can theoretically be achieved in the Kagome lattice [22], a rare structure composed of opposite top triangular lattices, which can be regarded as a type of deformation of honeycomb lattice. The Kagome lattices of germanene and silicene with the FB structure can be fabricated on an Al(111) substrate [23, 24]. Additionally, germanene with a honeycomb lattice can also be fabricated on an Al(111) substrate without an alloy layer [25]. Silicon (Si), germanium (Ge) and antimony (Sb) are located in adjacent places in the periodic table of elements and all belong to semimetals.

Inspired by the reviewed pioneering research, here we report on the first synthesis of β -Sb on an Al(111) substrate without an alloy layer, first observation of

antimonene in the Kagome lattice that have not been predicted before, we conducted a measurement of a Dirac node at Γ near -1.2 eV and achieved the inaugural experimental demonstration of antimonene's status as a topological insulator. Furthermore, we theoretically clarified the type of interaction and band structure in bulk state, and demonstrated the FB structure exists in this 2D material.

2.Experimental section

The cell structure of a single aluminum crystal is face-centered cubic with lattice constant of 4.04Å. Al(111) exhibits hexagonal symmetry with 1×1 surface reconstruction [26], as shown in Fig. 1f. The Al(111) substrate is cleaned through cycles of Ar^+ sputtering and annealing at 550°C. The resulting flat and wide substrate surface is observed using a scanning tunneling microscope (STM), as depicted in Fig. 1c. STM [27] spectra are acquired at 77 K under an ultra-high vacuum of 1×10^{-10} mbar using an STM chamber provided by Createc. The obtained STM images are processed using WSxM software. Based on the height profile, no island impurities or vacancies are observed on the substrate surface after annealing. Consequently, sharp diffraction patterns shown in Figs. 1a and 1b can be observed using a high-energy electron diffractometer (RHEED). Two diffraction patterns correspond to incident angles that differ by 30°. Following the zone law, the RHEED diffraction patterns furnish insights into the reciprocal lattice [28], indicating that the $[1\bar{1}0]$ and $[2\bar{1}\bar{1}]$ crystal orientations correspond to narrow and wide stripes, respectively, as depicted in Figs. 1a and 1b.

Once a clean Al(111) substrate is obtained, Sb atoms are evaporated from an effusion cell [29]. The temperature of Sb source shown in control panel maintained at 350°C. The growth chamber of the MBE system is maintained at room temperature under ultra-high vacuum conditions (1×10^{-10} mbar). This study focuses on investigating the changes in the Sb atomic structure during an 8-minute deposition process to ensure the growth of a well-crystallized Sb epitaxial layer. STM results of Sb atoms deposited on Al(111) are shown in Figs. 1g–1j. Various ordered structures are formed automatically during deposition, but only one distinct RHEED diffraction

pattern is observed, as shown in Figs. 1d and 1e.

During the initial stages of deposition (≤ 2 min), Sb atoms exist as discrete clusters on the substrate. At this juncture, the interaction between Sb atoms and the outermost Al atoms is comparatively weaker than the interaction between individual Sb atoms themselves. As a result, Sb atoms exhibit an affinity to aggregate and can not form a 2D structure. With deposition time extending to 4 min, the observed RHEED patterns shown in Fig. 1d and 1e signify the emergence of a honeycomb lattice structure, marking the transition from a disordered Sb arrangement to an organized phase. This honeycomb lattice structure spontaneously forms at room temperature, and a clear demarcation is discernible between the disordered region and the honeycomb lattice, as shown in Figs. 1h and 1i. It is worth noting that this atomic edge structure of the honeycomb lattice is neither zigzag nor armchair [30] but a special cubic edge structure. After 6 minutes of deposition time, the previously vacant centers within the honeycomb structure become occupied by newly deposited Sb atoms. This results in a transition to a dice lattice structure [31], as illustrated in Figs. 1i and 1j, where both the honeycomb and dice lattices coexist. Ultimately, at 8 min, Monolayer of island-like Kagome lattice are stacked onto the dice lattice structure illustrated in Figs. 1j. Even after elevating the sample temperature to the annealing temperature of the Al(111) substrate, the observed RHEED patterns in Figs. 1d and 1e remained present, signifying the stability of antimonene as temperature increases. The alterations in composition during deposition, as measured via X-ray photoelectron spectroscopy (XPS), are depicted in Fig. S1 and summarized in Table S1. The core-level spectra of Sb 4d [32] and Al 2p [33], obtained using an aluminum K_{α} excitation source in XPS, are consistent with the STM images.

3.Results and discussion

Different phases of antimonene can be identified using STM, while only one type of RHEED pattern is observed, as shown in Figs. 1d and 1e. Based on the STM images and the profile line in Figs. 2b and 2g, a cubic lattice consisted of Sb atoms is identified above the outermost substrate surface as a buffer layer, explaining the

unique atomic edge structure observed in Figs. 1h and 1i.

The diffraction patterns of both Al(111) and the Sb monolayer can be simultaneously visualized on the fluorescent screen. The $1/3$ diffraction stripes correspond to three times the interplanar spacing of $\{1\bar{1}0\}$ or $\{2\bar{1}\bar{1}\}$, matching the lattice constants of 8.48\AA and 4.90\AA , as shown in Figs. 2e and 2f. The $3/2$ times interplanar spacing of $\{1\bar{1}0\}$ or $\{2\bar{1}\bar{1}\}$ in the cubic lattice, depicted in Figs. 2d and 2g correspond to the $2/3$ diffraction stripes, which precisely overlap with the $1/3$ diffraction stripes. The Sb monolayer's RHEED patterns along distinct incident directions overlap with the preceding substrate's diffraction patterns. Based on these observations, we propose that the most plausible atomic structure entails the honeycomb lattice (orange layer) being adsorbed on the top site of the Al(111) 3×1.5 -Sb cubic lattice (purple layer) above Al(111) substrate, as illustrated in Fig. 2h.

The adsorption site between Kagome and dice lattice can be determined through the STM image presented in Fig. 3b. During the deposition process, the lattice constant of the Sb monolayer is $3/2$ times the interplanar spacing of $\{1\bar{1}0\}$ and $\{2\bar{1}\bar{1}\}$, which also enables it to overlap with the $1/3$ diffraction stripes. As a result, various phases of antimonene can be distinguished using STM, but each phase corresponds to only one type of RHEED pattern, as illustrated in Figs. 1d and 1e.

First-principles calculations were performed using the projector augmented wave method [34] with the Perdew, Burke, and Ernzerhof functional [35] within the generalized gradient approximation (GGA) [36, 37], implemented in the Vienna ab initio simulation package (VASP) [38]. The section of Al(111) supercell was $8.48\times 7.35\times 20\text{\AA}$ in three dimensions, encompassing three atomic layers and a vacuum layer. The Al(111) section was relaxed before placing the Sb atoms on the surface. The positions of the Al atoms in the bottom layer were fixed during the optimization process, while the cutoff energy of the plane-wave basis set was set to 600 eV. The relaxed calculations were performed using a Gaussian smearing scheme with Γ -Centered $7\times 7\times 1$ K -mesh. The convergence criteria for the total (free) energy change and the maximum force on each atom were set to 1×10^{-5} eV and 0.02 eV/ \AA , respectively.

The properties of bonds in the lattice are determined by the chemical environment, and the electron localization function (ELF) [39] provides insight into the distribution of electron clouds between atoms [40] to ascertain the type of interaction. Whether deposited atoms can form the ordered structure or alloy, depend on the size and type of interaction between the atoms. The ELF analysis in Fig. 4 shows that the electron cloud around the Sb atoms remains delocalized, indicating that the Sb atoms above the Al(111) substrate have closed full-shell configurations, therefore, the electronic properties of antimonene are not affected by the substrate. The interaction between these Sb atoms and the Al atoms in the outermost layer of the substrate corresponds to a resonant valence state, an intermediate type of interaction between covalent and ionic bonds. Additionally, the Coulomb force dominates the interaction between Sb atoms in the horizontal plane. These findings further support the configuration of the Sb atoms shown in Fig. 1g.

To clarify the band structure of the honeycomb lattice, a high-symmetry path was chosen based on its rotational symmetry, which is equivalent to that of β -Sb in the free-standing state [18]. Similarly, for the Kagome lattice, the high-symmetry path selection was based on a method used to calculate the Kagome lattice of silicene epitaxially grown on Al(111) substrates [24]. The crystal point groups associated with the honeycomb lattice, dice lattice, and Kagome lattice are all categorized as D6h. The calculated band structures in bulk state, obtained through static calculations, are shown in Figs. 5a and 5b, where different colors represent the contributions from different orbitals. Both the honeycomb and Kagome lattices exhibit orbital hybridization.

According to Bloch's theorem [43], energy levels in isolated atoms convert into energy bands as electrons move coherently within the periodic potential of a crystal. The motion of electrons near the Fermi level, with high energy in the outermost shells, typically results in a high degree of dispersion in the band structure and a lower density of states (DOS) than the more localized electrons in the inner shells. The lattice structure and quantum interference effects are crucial in determining the electron motion. In the case of confined fermions or bosons in a Kagome lattice with

only nearest-neighbor hopping, completely destructive quantum interference occurs. This leads to a flat dispersion relation for trapped particles [22]. Consequently, the energy of electrons near the Fermi level in Sb atoms, as shown in Fig. 5b, exhibits minimal variation with changes in the wave vector position, resulting in a low dispersion flat band (FB) structure with a high DOS near the Fermi level. In FB structure, electrons have a highly localized characteristic that enhances their interaction effects with each other. Their motion is influenced by fewer scattering effects, making it challenging for hemispherical electron analyzers to capture a good signal-to-noise ratio. However, this also leads to the display of unique behaviors in the electronic transport properties of FB systems, such as extremely high mobility, very low resistivity, strong correlation effects, and Wigner crystals [44].

To experimentally investigate the energy dispersion along the M - Γ - M direction, angle-resolved photoemission spectroscopy (ARPES) [45] measurements were conducted using an Omicron apparatus equipped with a He I light source at temperature of 7 K and pressure of 3×10^{-11} mbar. The ARPES spectrum in Fig. 5c remains consistent for deposition times less than 10 min, the band crossing at the Γ point below the Fermi level at around -1.2 eV shown in Fig. 5c are known as Dirac point. The linear relation of Dirac point results in highly conductive properties in boundary state [46], which enables the robustness of helical boundary modes even in the presence of defects in the cubic atomic edge states depicted in Figs. 1h and 1i. The explanation for the occurrence of Dirac points in the honeycomb lattice can be provided by the Haldane model [47]. This model posits that the nontrivial topological properties of band structure originate from the breaking of time-reversal symmetry induced by next-nearest-neighbor hopping, and the experimental confirmation of Dirac points in graphene [48] further corroborated the Haldane model.

However, graphene in intrinsic state is limited in the applications of next-generation electronic devices due to its characteristic of having a zero band gap, in order to create a band gap, introducing spin-orbit coupling (SOC) can presents a strategy. In contrast to graphene, antimonene exhibits a stronger SOC effect, manifesting as a double-peak split in the Sb $4d$ energy spectrum shown in Fig. S1.

According to the Kane-Mele model [49], the introduction of spin-orbit coupling leads to a non-zero Z_2 topological number in antimonene, thereby giving rise to special topological boundary states. The topological number of the band structure can be expressed as an integral along the boundaries of the first Brillouin zone. The opposite edges of the first Brillouin zone differ only by a reciprocal lattice vector. According to the Bloch theorem, this equivalence is reflected in the wave function, where the expression of electronic states between opposite edges differs by only a phase factor, satisfying U(1) gauge transformation [46].

In the case of trivial topology, the exponent of the phase factor remains constant. Therefore, when integrating along a closed loop throughout the Brillouin zone, the Chern number is zero. However, when the exponent of the phase factor between opposite edges varies with the position coordinates in reciprocal space, circling around the boundaries of the first Brillouin zone leads to non-cancellation of contributions between opposite edges, resulting in a non-zero topological number, indicating a non-trivial band structure that analogous to a Möbius strip [50], where after circling it, a phase difference exists. The singularity of the Möbius strip corresponds to the band structure at the Dirac point, shown as Fig. 5d.

In this context, the experimental results depicted in Figs. 5c and 5d proved that antimonene on Al(111) behaves as a 2D topological insulator experimentally. It is worth mentioning that measuring the boundary state of a 2D topological insulator using ARPES is more challenging than measuring the surface state of a 3D topological insulator, such as the topological surface state of Bi_2Se_3 [51], due to the difficulty of obtaining ordered $E-k$ relationships from photoelectrons emitted from the edge of a 2D material. However, if the 2D material possesses well-defined atomic edge states, as illustrated in Figs. 1h and 1i, the measurement becomes feasible.

In addition, the low dispersion relation and highly localized electronic states of FB structure shown in Figs. 5a and 5b facilitate the formation of topological insulator boundary states within the energy gap while maintaining their topologically protected properties. Furthermore, since the kinetic energy of electronic states within the FB structure is small and exhibits a strong localization, the boundary states are more

likely to form within the energy gap and possess higher resistance to localized perturbations.

4. Conclusions

Various phases of antimonene, including the previously unpredicted Kagome lattice structure, can be synthesized on an Al(111) substrate at room temperature without an alloy layer. ARPES measurements reveal the presence of a Dirac cone below the Fermi level at approximately -1.2 eV in the boundary state, first demonstrated that antimonene exhibits characteristics of 2D topological insulators in experimental, thereby offering great potential for developing next-generation electronic devices. Furthermore, DFT calculations demonstrate the delocalization of electrons in bulk state, corresponding to the FB structure with low dispersion and high DOS near the Fermi level in the bulk state of antimonene on Al(111), and the FB structure enables the boundary states tend to emerge within the energy gap, making them robust against localized perturbations. In summary, antimonene on Al(111) represents a 2D topological insulator with a helical boundary modes and a low dispersion electronic structure with high DOS near the Fermi level in the bulk state.

Appendix A. Supplementary Material

To clarify the change of chemical environment during the deposition, in order to describe the interaction between antimonene monolayer and substrate in experimental, we characterized the binding energy of Sb *4d* and Al *2p* core-level spectra by XPS.

AUTHOR DECLARATIONS

Conflict of Interest

The authors have no conflicts to disclose

Data availability

The data that support the findings of this research will be made available on

request.

References

- [1] Novoselov K S, Geim A K, Morozov S V, Jiang D, Zhang Y, Dubonos S V, Grigorieva I V and Firsov A A, Electric Field Effect in Atomically Thin Carbon Films, 2004 *Science* **306** 666–9
- [2] Novoselov K S, Geim A K, Morozov S V, Jiang D, Katsnelson M I, Grigorieva I V, Dubonos S V and Firsov A A, Two-dimensional Gas of Massless Dirac Fermions in Graphene, 2005 *Nature* **438** 197–200
- [3] Kane C L and Mele E J, Quantum Spin Hall Effect in Graphene, 2005 *Phys Rev Lett.* **95** 226801
- [4] Wang J-Y, Deng S-B, Liu Z-F and Liu Z-R, The Rare Two-dimensional Materials with Dirac Cones, 2005 *Natl Sci Rev.* **2** 22–39
- [5] Zhang S-L, Xie M-Q, Li F-Y, Yan Z, Li F-Y, Kan E, Liu W, Chen Z-F and Zeng H-B, Semiconducting Group 15 Monolayers: A Broad Range of Band Gaps and High Carrier Mobilities, 2016 *Angew. Chem. Int. Ed.* **55** 1666–9
- [6] Li L-K, Yu Y-J, Ye G-J, Ge Q-Q, Ou X-D, Wu H, Feng D-L, Chen X-L and Zhang Y-B, Black Phosphorus Field-effect Transistors, 2014 *Nat Nanotechnol.* **9** 372–7
- [7] Zhang J-L, Zhao S-T, Han C, Wang Z-Z, Zhong S, Sun S, Guo R, Zhou X, Gu C-D and Yuan K-D, *et al*, Epitaxial Growth of Single Layer Blue Phosphorus: A New Phase of Two-Dimensional Phosphorus, 2016 *Nano Lett.* **16** 4903–8
- [8] Zhang S-L, Yan Z, Li Y-F, Chen Z-F and Zeng H-B, Atomically Thin Arsenene and Antimonene: Semimetal-semiconductor and Indirect-direct Band-gap Transitions. 2015 *Angew. Chem. Int. Ed.* **54** 3112–5
- [9] Carrasco J S, Congost-Escoin P, Assebban M and Abellán G, Antimonene: a tuneable post-graphene material for advanced applications in optoelectronics, catalysis, energy and biomedicine. 2023 *Chem. Soc. Rev.* **52** 1288–330
- [10] Reis F, Li G, Dudy L, Bauernfeind M, Glass S, Hanke W, Thomale R, Schäfer J and Claessen R, Bismuthene on a SiC Substrate: A Candidate for a New High-temperature Quantum Spin Hall Material, 2017 *Science* **357** 287–90
- [11] Wang G-X, Pandey R and Karna S P, Atomically Thin Group V Elemental Films: Theoretical Investigations of Antimonene Allotropes, 2015 *Acs Appl Mater.* **7** 11490–6
- [12] Ji J-P, Song X-F, Liu J-Z, Yan Z, Huo C-X, Zhang S-L, Su M, Liao L, Wang W-H, Ni Z-H, Hao Y-F and Zeng H-B, Two-dimensional Antimonene Single Crystals Grown by van der Waals Epitaxy, 2016 *Nat Commun.* **7** 13352–60
- [13] Shao Y, Liu Z-L, Cheng C, Wu X, Liu H, Liu C, Wang J-O, Zhu S-Y, Wang Y-Q, Shi and D-X, *et al*, Epitaxial Growth of Flat Antimonene Monolayer: A New Honeycomb Analogue of Graphene, 2018 *Nano Lett.* **18** 2133–9
- [14] Zhu S-Y, Shao Y, Wang E, Cao L, Li X-Y, Liu L-Z, Liu C, Liu L-W, Wang J-O, Ibrahim O, Sun J-T, Wang Y-L, Du S-X and Gao H-J, Evidence of Topological Edge States in Buckled Antimonene Monolayers, 2019 *Nano Lett.* **19** 6323–9

- [15] Cantero E D, Martínez E A, Serkovic-Loli L N, Fuhr J D, Grizzi O and Sánchez E A, Synthesis and Characterization of a Pure 2D Antimony Film on Au(111), 2021 *J. Phys. Chem. C*. **125** 9273–80
- [16] Sun S, Yang T, Luo Y-Z, Gou J, Huang Y-L, Gu C-D, Ma Z-R, Lian X, Duan S-S and Andrew T S W, *et al*, Realization of a Buckled Antimonene Monolayer on Ag(111) via Surface Engineering, 2020 *J Phys Chem Lett*. **11** 8976–82
- [17] Zhang P, Ma C, Sheng S-X, Liu H, Gao J-S, Liu Z-J, Cheng P, Feng B-J, Chen L and Wu K-H, Absence of topological β -antimonene and growth of α -antimonene on noble metal Ag(111) and Cu(111) surfaces, 2022 *Phys. Rev. Mater.* **6** 074002
- [18] Radha S K and Lambrecht W R L, Topological Band Structure Transitions and Goniopolar Transport in Honeycomb Antimonene as a Function of Buckling, 2020 *Phys Rev B*. **101** 235111
- [19] Zhao M-W, Zhang X-M and Li L-Y, Strain-driven Band Inversion and Topological Aspects in Antimonene, 2015 *Sci Rep*. **5** 16108
- [20] Hasan M Z and Kane C L, Colloquium: Topological Insulators, 2010 *Rev Mod Phys*. **82** 3045–67
- [21] Sun K, Gu Z-C, Katsura H and Sarma S D, Nearly Flatbands with Nontrivial Topology, 2011 *Phys Rev Lett*. **106** 236803
- [22] Li Z, Zhuang J-C, Wang L, Feng H-F, Gao Q, Xu X, Hao W-C, Wang X-L, Zhang C and Wu K-H, *et al*, Realization of Flat Band with Possible Nontrivial Topology in Electronic Kagome Lattice, 2018 *Sci Adv*. **4** eaau4511
- [23] Kubo O, Kinoshita S, Sato H, Miyamoto K, Sugahara R, Endo S, Tabata H, Okuda T and Katayama M, Kagome-like Structure of Germanene on Al(111), 2021 *Phys Rev B*. **104** 085404
- [24] Sassaa A, ohanssonb F O L, Lindblad A, Yazdic M G, Simonovb K, Weissenriederc J, and Muntwilerd M, Iyikanate F, Sahinf H, and Angotg T, *et al*, Kagome-like Silicene: A Novel Exotic Form of Two-dimensional Epitaxial Silicon, 2020 *Appl Surf Sci*. **530** 147195
- [25] Derivaz M, Dentel D, Stephan R, Hanf M C, Mehdaoui A, Sonnet P and Pirri C, Continuous Germanene Layer on Al(111), 2015 *Nano lett*. **15** 2510–6
- [26] Wintterlin J, Wiechers J, Brune H, Gritsch T, Höfer H and Behm R J, Atomic-resolution Imaging of Close-packed Metal Surfaces by Scanning Tunneling Microscopy, 1989 *Phys Rev Lett*. **62** 59–62
- [27] Binnig G and Rohrer H, Scanning Tunneling Microscopy, 2000 *IBM J. Res. Develop*. **44** 279–93
- [28] Peng L-M, Dudarev S L and Whelan M J, Electron Scattering Factors of Ions and Dynamical RHEED From Surfaces of Ionic Crystals, 1998 *Phys Rev B*. **57** 7259–65
- [29] Shukla, A K, Banik S, Dhaka R S, Biswas C, Barman S R and Haak H, Versatile UHV Compatible Knudsen Type Effusion Cell, 2004 *Rev Sci Instrum*. **75** 4467–70
- [30] Wang Y-L and Ding Y, Electronic Structure and Carrier Mobilities of Arsenene and Antimonene Nanoribbons: A First-Principle Study, 2015 *Nanoscale Res Lett*. **10** 254–64
- [31] Kotecký R, Salas J and Sokal A D, Phase Transition in the Three-State Potts Antiferromagnet on the Diced Lattice, 2008 *Phys Rev L*. **101** 030601
- [32] Morgan D J, Metallic antimony (Sb) by XPS, 2017 *Surf. Sci. Spectra*. **24** 024004

- [33] McCafferty E and Wightman J P, Determination of the concentration of surface hydroxyl groups on metal oxide films by a quantitative XPS method, 1998 *Surf Interface Anal.* **26** 549–64.
- [34] Perdew J P, Burke K and Ernzerhof M, Generalized Gradient Approximation Made Simply, 1996 *Phys Rev Lett.* **77** 3865–8
- [35] Blöchl P E, Projector Augmented-wave Method, 1994 *Phys Rev B Condens Matter.* **50** 17953–79
- [36] Perdew J P, Chevary J A, Vosko S H, Jackson K A, Pederson M R, Singh D J and Fiolhais C, Atoms, Molecules, Solids, and Surfaces: Applications of the Generalized Gradient Approximation for Exchange and Correlation, 1993 *Phys Rev B.* **46** 6671–87
- [37] Langreth C D and Mehl M J, Beyond the Local-density Approximation in Calculations of Ground-state Electronic Properties, 1983 *Phys Rev B.* **28** 1809–34
- [38] Kresse G, Ab initio Molecular Dynamics for Liquid Metals, 1995 *J Non-cryst Solids.* **192**, **193** 222–9
- [39] De Santis L and Resta R, Electron Localization at Metal Surfaces, 2000 *Surf Sci.* **450** 126–32
- [40] Becke A D and Edgecombe K E, A Simple Measure of Electron Localization in Atomic and Molecular Systems, 1990 *J. Chem. Phys.* **92** 5397–403
- [41] Wang V, Xu N, Liu J-C, Tang G and Geng W T, VASPKIT: A User-friendly Interface Facilitating High-throughput Computing and Analysis Using VASP Code, 2019 *Comput Phys Commun.* **267** 108033
- [42] Zhang P, Richard P, Qian T, Xu Y-M, Dai X and Ding H, A Precise Method for Visualizing Dispersive Features in Image Plots, 2011 *Rev Sci Instrum.* **82** 043712
- [43] Bloch V F, über die Quantenmechanik der Elektronen in Kristallgittern, 1928 *ZS. f. Phys.* **52** 555–99
- [44] Wu C, Bergman D, Balents L and Das Sarma S, Flat Bands and Wigner Crystallization in the Honeycomb Optical Lattice, 2007 *Phys Rev Lett.* **99** 070401
- [45] Damascelli A, Probing the Electronic Structure of Complex Systems by ARPES, 2004 *Phys Scr.* **T109** 61–74
- [46] Ando Y, Topological Insulator Materials, 2013 *J Phys Soc Jpn.* **82** 102001
- [47] Haldane F D M, Model for a Quantum Hall Effect without Landau Levels: Condensed-Matter Realization of the "Parity Anomaly", 1988 *Phys Rev Lett.* **61** 2015–8
- [48] Zhang Y-B, Tan Y-W, Stormer H L and Kim P, Experimental observation of the quantum Hall effect and Berry's phase in graphene, 2005 *Nature* **438** 201–4
- [49] Kane C L and Mele E J, Z_2 Topological Order and the Quantum Spin Hall Effect, 2005 *Phys Rev Lett.* **95** 146802
- [50] Haldane C. M., Topological Insulators: A Romance with Many Dimensions, 2010 *Nat. Nanotechnol.* **5** 477–9
- [51] Kim S, Ye M, Kuroda K, Yamada Y, Krasovskii E E, Chulkov E V, Miyamoto K, Nakatake M, Okuda T and Ueda Y, *et al*, Surface Scattering via Bulk Continuum States in the 3D Topological Insulator Bi_2Se_3 , 2011 *Phys Rev Lett.* **107** 056803

FIGURES AND FIGURE CAPTIONS

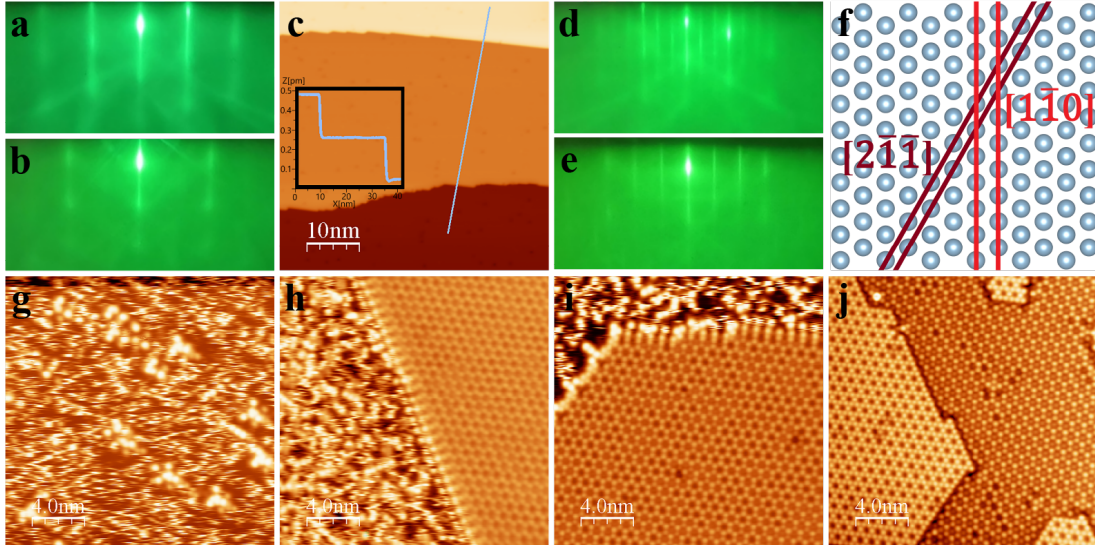


Figure. 1. Experimental process applied to the Al(111) substrate which presents high-resolution STM images that depict the evolution of surface topography over time and RHEED diffraction patterns. (a and b) RHEED diffraction pattern of Al(111) surface along the crystal orientation of $[1\bar{1}0]$ and $[2\bar{1}\bar{1}]$ respectively. (c) 50nm \times 50nm large scale STM image of Al(111) substrate with $V_b=1\text{V}$ and $I_t=100\text{pA}$. Inset: A height profile along the blue line at the terrace edge, the height corresponds to the intrinsic height of Al(111) terrace is around 2.5pm. (d and e) New diffraction pattern along $[1\bar{1}0]$ and $[2\bar{1}\bar{1}]$ respectively. (f) The model of aluminum single crystal in the section of (111) plane. (g) 20nm \times 20nm STM image with $V_b=0.5\text{V}$ and $I_t=500\text{pA}$ for 2 min deposition. (h) 20nm \times 20nm STM image with $V_b=0.4\text{V}$ and $I_t=500\text{pA}$ for 4 min deposition. (i) 20nm \times 20nm STM image with $V_b=0.5\text{V}$ and $I_t=600\text{pA}$ for 6 min deposition. (j) 20nm \times 20nm STM image with $V_b=0.5\text{V}$ and $I_t=310\text{pA}$ for 8 min deposition.

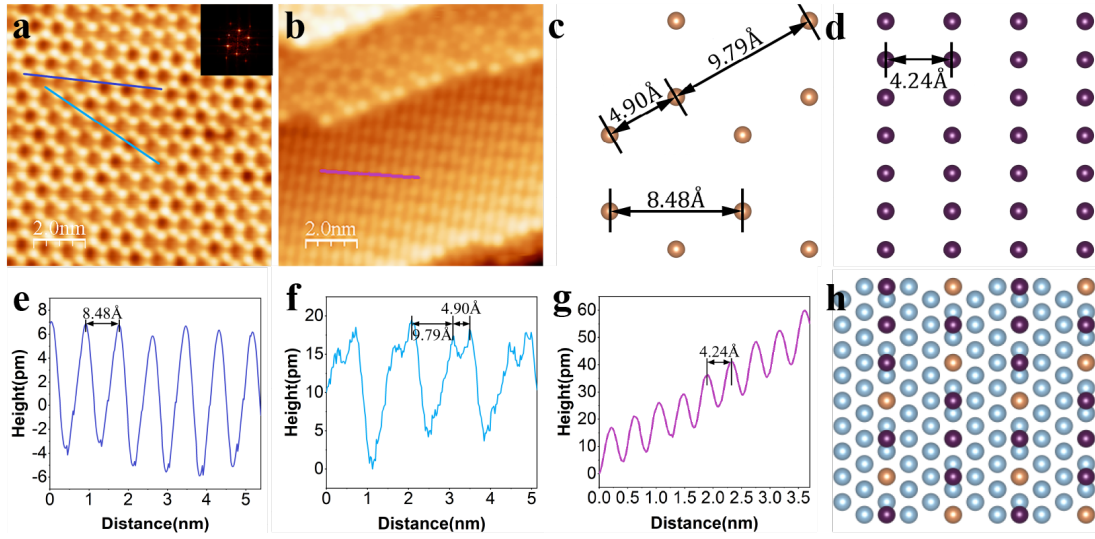


Figure. 2. The honeycomb lattice of Sb layer epitaxial growth on the Al(111) surface ascertained by RHEED and STM. (a) 10nm×10nm STM image of honeycomb lattice with $V_b=0.4\text{V}$ and $I_t=500\text{pA}$, and a Fast Fourier Transform (FFT) is included in the upper right corner. (b) 10nm×10nm STM image of Sb cubic lattice beneath the honeycomb or Dice layer with $V_b=0.5\text{V}$ and $I_t=600\text{pA}$ for 6 min deposition. (c and d) Top view of honeycomb and cubic lattice. (e and f) Profile along indigo line and turquoise line in (a) indicate that the lattice constants of honeycomb structure are around 8.48\AA , 9.79\AA and 4.90\AA respectively. (g) Height profile along the blue line in (b) indicate that the lattice constants of cubic layer are around 4.24\AA . (h) The honeycomb lattice adsorbed on the atomic arrangement of the Al(111) 3×1.5 -Sb cubic lattice above the Al(111).

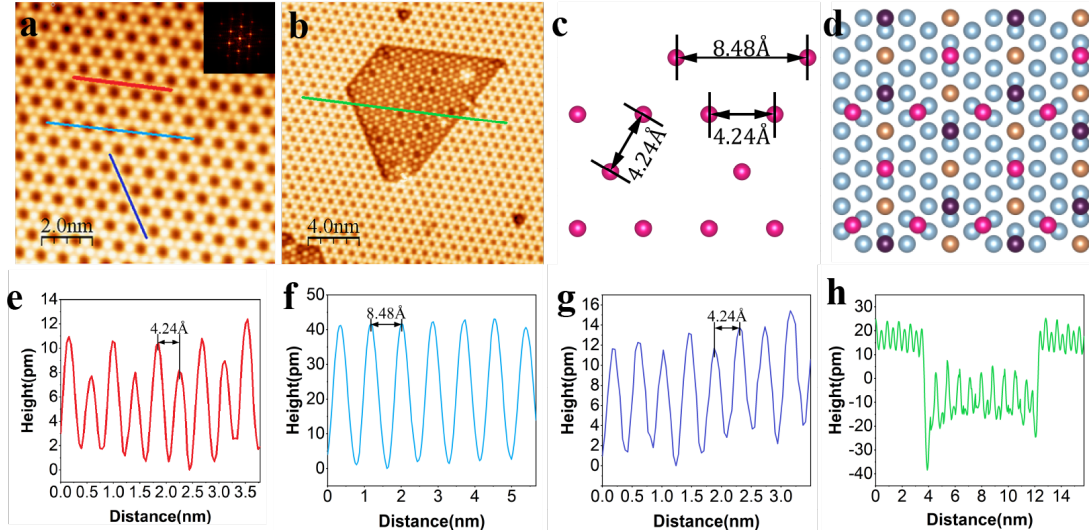


Figure. 3. Kagome lattice deposited above dice lattice. (a) 10nm×10nm STM image of Kagome lattice with $V_b=0.5\text{V}$ and $I_t=310\text{pA}$, and the FFT in the upper right corner. (b) 20nm×20nm STM image of Kagome lattice, dice lattice and honeycomb lattice simultaneous existence for 8 min deposition with $V_b=0.5\text{V}$ and $I_t=700\text{pA}$. (c) Top view of Kagome lattice. (d) The Kagome lattice of Sb atoms (pink layer) adsorbed on the bridge site of dice lattice layer (orange layer). (e, f and g) Profile along aqua green, turquoise and indigo line in (a) indicate that the lattice constants of Kagome structure are around 4.24Å, 8.48Å and 4.24Å respectively. (h) Profile along green line in (b) indicate the interplanar distance between Kagome and dice lattice are around 10pm.

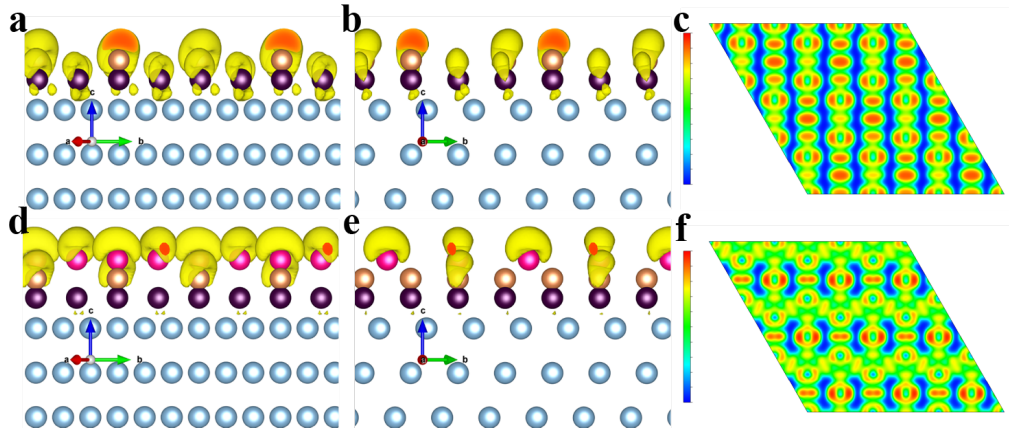


Figure. 4. ELF image of Sb honeycomb structure (upper) and Sb Kagome structure (lower) on Al(111) surface. (a and b) Side view image of honeycomb structure ELFCAR along a^* and a axis respectively. (c) ELFCAR isosurface of honeycomb structure sliced at the value of 1. (d and e) Side view image of Kagome structure ELFCAR along a^* and a axis respectively. (f) ELFCAR isosurface of Kagome structure sliced at the value of 1.

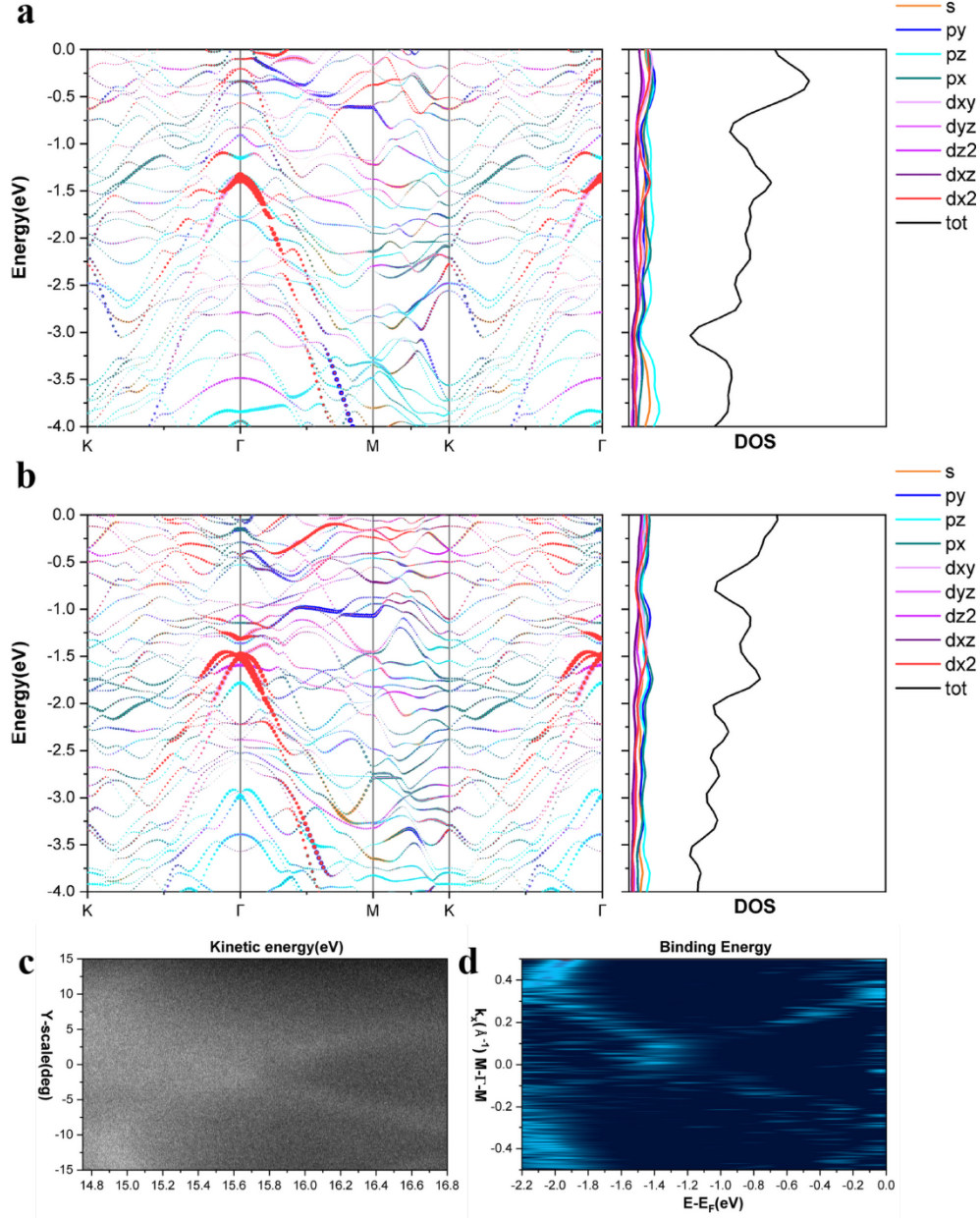


Figure. 5. Electronic structures of honeycomb and Kagome lattice. (a) and (b) show the band structure of honeycomb (upper) and Kagome (lower) lattice in bulk state respectively exported by vaspkit [41] with orbital projection, the right part shows the (P)DOS. (c) Energy-dispersion spectrum in boundary state with $h\nu=21.218\text{eV}$, and the horizontal axis starts from 14.75eV . (d) $E-k$ relationships using 2D curvature method [42] exported by Igor.